Phase-space foundations of electron holography

A. Lubk and F. Röder
Triebenberg Laboratory, Institute of Structure Physics, Technische Universität Dresden, 01062 Dresden, Germany
(Received 12 May 2015; published 23 September 2015)

We present a unified formalism for describing various forms of electron holography in quantum mechanical phase space including their extensions to quantum-state reconstructions. The phase-space perspective allows for taking into account partial coherence as well as the quantum mechanical detection process typically hampering the unique reconstruction of a wave function. We elaborate on the limitations imposed by the electron optical elements of the transmission electron microscope as well as the scattering at the target. The results provide the basis for vastly extending the scope of electron holographic techniques towards analyzing partially coherent signals such as inelastically scattered electrons or electron pulses used in ultrafast transmission electron microscopy.

DOI: 10.1103/PhysRevA.92.033844 PACS number(s): 42.40.−i, 41.75.Fr, 42.50.Dv, 42.40.Kw

I. INTRODUCTION

Holography was originally invented by D. Gabor [1] in an attempt to correct the, at that time, insurmountable spherical aberration of the objective lens of the transmission electron microscope (TEM) [2] by numerically removing the corresponding phase shift *a posteriori*. The holographic principle proved so general that it found its way into a wide variety of techniques, all aiming at exploiting the phase information of a wave field (not necessarily electrons) in one way or another (e.g., [3]). It turned out that in a multitude of cases the phase encodes the optical path length traversed by the wave, lending its significance to structure determination problems by x-ray diffraction [4,5], measurement of electromagnetic potentials by electron holography [6–9], or aberration assessment and correction in telescopes [10,11]. As realized by Gabor, holography is essentially nonlinear, that is, the reconstruction of a complex wave function from recorded intensities necessarily leads to some sort of root extraction. The associated ambiguities manifest as twin image problems [12–14], nonconverging holographic reconstruction algorithms [15], or nonunique wave reconstructions due to unknown boundary conditions [16] depending on the holographic technique. Consequently, large and ongoing efforts have been devoted to the mitigation of these problems. They are exacerbated further in the presence of partial coherence, eventually hampering the reconstruction of a single wave function (or its phase). The most striking electron holographic reconstructions have therefore been obtained with highly coherent illumination and setups allowing for unambiguous wave reconstruction (e.g., [17–19]).

As a further product of these investigations, a number of linear reconstruction schemes avoiding the issue of nonlinearity have been developed [20,21]. These so-called quantum-state measurements seek a reconstruction of a more general object: a preferably complete representation of the density operator. Here, we elaborate on this change of perspective, that is, we consider electron holography as a phase-space reconstruction instead of a phase reconstruction [22,23]. We thereby circumvent any problems related to partial spatial coherence and nonlinearities and obtain a unified description of various holographic methods including related concepts such as superresolution techniques. The unified framework allows for discussing and comparing the requirements, the area of application, and generalizations of different types of electron holography. We restrict ourselves to the most popular methods in transmission electron microscopy (see [24] for an overview), namely, off-axis holography [9,25], in-line holography [12,26–31], differential phase contrast (DPC) [16,32–34], and ptychography [35–38]. With some slight modifications, however, the results also apply to related holographic techniques, for example, those pertaining to the flourishing field of x-ray holography.

II. QUANTUM MECHANICAL PHASE-SPACE DESCRIPTION OF THE ELECTRON BEAM

In order to provide the framework for a phase-space description of holography we shortly introduce some basic concepts of a quantum measurement. A mixed state, i.e., a partially coherent wave field, can be generally described by the density operator

$$\begin{aligned}\hat{\rho} &= \sum_n P_n |\Psi_n\rangle\langle\Psi_n| \\ &= \int \mathrm{d}x\,\mathrm{d}x' \underbrace{\sum_n P_n \langle x|\Psi_n\rangle\langle\Psi_n|x'\rangle}_{\rho(x,x')=\rho^*(x',x)} |x\rangle\langle x'|, \end{aligned} \tag{1}$$

where P_n are the probabilities in the diagonal basis $|\Psi_n\rangle$ and $\rho(x,x')$ is the position-space matrix element of the density operator referred to as the density matrix. Here and in the following we focus on the one-dimensional (1D) position space for brevity and clarity. The two-dimensional (2D) case, indicated by boldface-vector-valued coordinates, is discussed occasionally if necessary. The above definition allows for computation of the outcome of any measurement on some observable $\hat{A}$ in a partially coherent system by the following trace:

$$\langle A\rangle_{\hat{\rho}} = \mathrm{Tr}(\hat{\rho}\hat{A}). \tag{2}$$

In particular, the detected intensity in the image plane of a TEM reads

$$I(r) = \rho(x = r, x' = r). \tag{3}$$

The Wigner function is another representation of the density operator, obtained by Fourier transforming the density matrix

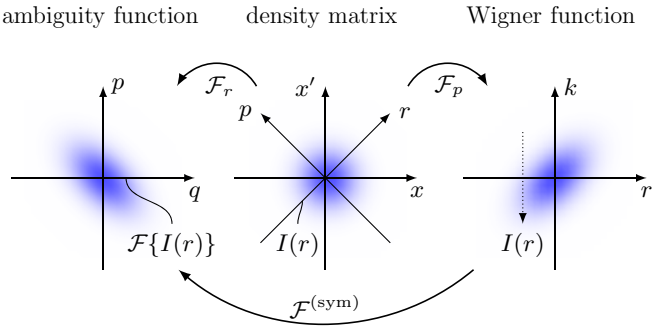

FIG. 1. (Color online) Different representations of the density operator as the ambiguity function, density matrix, and Wigner function. The relation among the three representations as well as the outcome of an intensity measurement is indicated.

along the antidiagonal elements (determining the coherence; Fig. 1):

$$W(r,k) = \frac{1}{2\pi}\int \mathrm{d}p \left\langle r - \frac{1}{2}p\middle|\hat{\rho}\middle|r + \frac{1}{2}p\right\rangle e^{-ikp}. \quad (4)$$

Here and in the following we use Hartree atomic units ($m_e = e = \hbar = 1$). The Wigner function is a particular representative of real-valued quantum mechanical phase-space densities or quasiprobability functions [39]. It is particularly well suited to describe the optical transfer in the TEM for various reasons detailed below [40]. First, its marginal distributions (Fig. 1),

$$I(r) = \int W(r,k)\mathrm{d}k, \quad I(k) = \int W(r,k)\mathrm{d}r, \quad (5)$$

yield directly the measured intensities in the image and diffraction plane in the TEM. Furthermore, the first moment of the Wigner function along the momentum coordinate corresponds to the probability current

$$j(r) = \int k W(r,k)\mathrm{d}k, \quad (6)$$

and one may define generalized currents in the following way:

$$j^{(n)}(r) = \int k^n W(r,k)\mathrm{d}k. \quad (7)$$

A very general measure of coherency, the quantum mechanical purity, defined by the ratio between the minimal attainable phase-space volume 2π and the actual volume Ω, is given by the phase-space integral of the squared Wigner function of the (normalized) quantum state according to

$$\zeta = \frac{2\pi}{\Omega} = 2\pi \iint \mathrm{d}r\mathrm{d}k\, W^2(r,k) \leqslant 1. \quad (8)$$

This formula is a special case of the more general relation

$$\mathrm{Tr}\left(\hat{\rho}\hat{A}\right) = \int_{-\infty}^{\infty}\mathrm{d}x \int_{-\infty}^{\infty}\mathrm{d}k A(x,k) W_{\hat{\rho}}(x,k), \quad (9)$$

yielding the expectation value of an arbitrary operator through a phase-space integral of the corresponding Wigner transform,

$$A_W(r,k) = \int \mathrm{d}p \left\langle r - \frac{1}{2}p\middle|\hat{A}\middle|r + \frac{1}{2}p\right\rangle e^{-ikp}, \quad (10)$$

of that operator.

When discussing electron holography further below, we frequently make use of the (symplectic) Fourier transform ($\mathcal{F}^{(\mathrm{sym})}$) of the Wigner function along both phase-space coordinates (Fig. 1),

$$\tilde{W}(q,p) = \frac{1}{2\pi}\int W(r,k)e^{-iqr}e^{ikp}\mathrm{d}r\mathrm{d}k, \quad (11)$$

which is referred to as Moyal's characteristic function or the ambiguity function in the literature. Inserting the definition of the Wigner function, one readily obtains that the ambiguity function corresponds to the Fourier transform of the density matrix along the main diagonal

$$\tilde{W}(q,p) = \frac{1}{2\pi}\int \rho\left(r - \frac{1}{2}p, r + \frac{1}{2}p\right)e^{-iqr}\mathrm{d}r, \quad (12)$$

instead of the antidiagonal as in the case of the Wigner function. Owing to the above definition, the diffractogram (i.e., the Fourier transform of image intensity) is given by the cross section of the ambiguity function,

$$\mathcal{F}\{I(r)\} = \tilde{W}(q, p = 0), \quad (13)$$

which may be generalized to all moments of the Wigner function as

$$\mathcal{F}\left\{\int k^n W(r,k)\mathrm{d}k\right\} = i^n \frac{\partial^n}{\partial p^n}\tilde{W}(q,p)\bigg|_{p=0}. \quad (14)$$

A quantum state represented by some density operator is determined if one of the equivalent representations of the density operator (Fig. 1) is completely known. Measurement schemes seeking this quantum state are referred to as quantum-state reconstructions and we show below that the well-known electron holographic schemes can be discussed within that framework. Because any measurement on the quantum state implies taking a certain trace, cross section, or projection, depending on the respective representation, quantum-state measurement necessarily requires the preparation of a large number of identical states ("the quorum" [41,42]) to eventually synthesize its complete shape. Therefore, no matter which holographic scheme is considered, its extension to quantum-state reconstruction requires repeatedly acquiring electron micrographs under different conditions.

Two preliminary remarks, one concerning the optical transfer (the imaging process) within the TEM and the second considering the nature of the scattering process in the sample, are essential before starting a discussion of the various holographic techniques. When recording the quorum the imaging conditions are altered, because varying one particular imaging parameter, such as the defocus, is an essential part of the holographic technique. This change typically introduces unwanted side effects, such as parasitic aberrations, modifying the quantum state such that the quorum does not consist of identical quantum states anymore. These effects have to be taken into account when performing an experimental quantum-state reconstruction, which is typically far from trivial and poses a formidable obstacle. Nevertheless, we focus on the theoretical framework here and only touch on these issues below.

Second, it will turn out that the concept of a quantum-state reconstruction can be significantly extended if the interaction of the electron beam and the sample in the TEM is of a

particularly simple form, that is, single axial scattering. This refers to an approximate description of the scattering valid for electrons scattered from sufficiently unordered potentials into small angles. This approximation is often applicable under medium-resolution imaging conditions (out-of-zone axis orientation, very small scattering angles) typically used for medium-resolution investigations. In this case the final density matrix of the electrons is obtained by a simple product of the incoming one with a mutual object transparency [43], which solely depends on the object and the energy loss ΔE involved in the interaction,

$$\rho_f(x,x';\Delta E) = T(x,x';\Delta E)\rho_i(x,x'). \tag{15}$$

In the case of purely elastic axial scattering of electrons at velocity v, the transparency

$$T_{\mathrm{el}}(x,x') = \exp\left(\frac{i}{v}\int(\Phi(x,z)-\Phi(x',z))\mathrm{d}z\right) \times \exp\left(-\frac{1}{2}\int(\mu_{\mathrm{el}}(x,z)+\mu_{\mathrm{el}}(x',z))\mathrm{d}z\right) \tag{16}$$

is separable into two wave transmission functions containing the projected electrostatic potential Φ as the phase argument and the projected elastic damping coefficient due to scattering into angles larger than the instrument's aperture stop as the amplitude argument. If the amplitude modulation can be neglected, one speaks of a pure phase object, and a particular simple relationship between the lateral gradient of the projected potential, i.e., the projected electric field E_x, and the probability current can be established [44]:

$$j(x,z) = -\frac{I}{v}\int E_x(x,z)\mathrm{d}z. \tag{17}$$

The "elastic" separability is usually lost when inelastic interaction is considered because the beam electrons become entangled with the object's degrees of freedom

$$T\left(x,x';\Delta E\right) = T_{\mathrm{el}}(x,x') \times \underbrace{\exp\left(-\frac{1}{2}\int\mu_{\mathrm{inel}}(x,x',z)\mathrm{d}z\right)}_{T_{\mathrm{inel}}(x,x';\Delta E)}. \tag{18}$$

Here, one widely employed approximation considering the dominant influence of bulk plasmon excitations reads

$$\mu_{\mathrm{inel}}(x,x',z) = \mu_{\mathrm{inel}}(|x-x'|,z), \tag{19}$$

which depends only on the distance between two spatial coordinates, when the plasma is considered isotropic and homogeneous [45]. We emphasize that under atomic resolution conditions both the contributions of electrons scattered into large angles and the systematic interference of electrons scattered at crystals oriented in zone axis cannot be described within the single axial scattering approximation (e.g., [46]). In this case the notion of a scalar-valued object transparency *function* T becomes invalid. Instead, the scattering is described by a scattering *operator*, which comprises the action of the scattering potential *and* the propagation of the electrons in between scattering events, which is completely neglected in single axial scattering. The framework for the computation of this scattering operator is provided by dynamic electron scattering theory (e.g., [47] and [48]), leading, e.g., to the iterative propagation of a pure state (an electron wave) by sequential application of transmission functions and Fresnel propagators referred to as the Multislice algorithm [49]. In order to facilitate a better comprehensibility, we only consider monoenergetic (monochromatic) quantum states in the following, that is, we assume a sufficiently perfect energy filter, when recording the signal. The energy dependency of the imaging process may be introduced by integrating over the energy interval considered in the experiment.

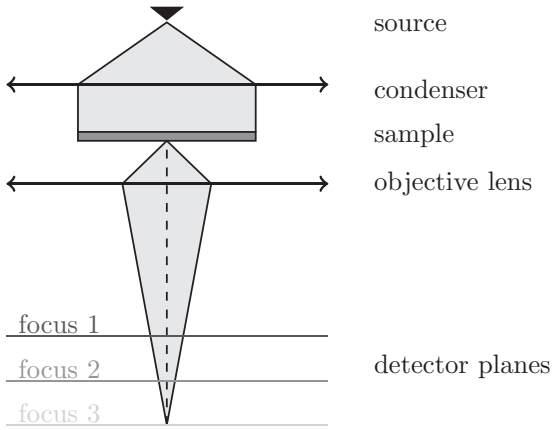

FIG. 2. Principle optical setup of in-line holography. Accordingly, the defocus interval is ideally bounded by the focal and image plane.

III. QUANTUM-STATE HOLOGRAPHY

A. In-line holography

In-line holography or focal series reconstruction in the typical setup employed in transmission electron microscopy intends to recover the electron wave function from a set of differently defocused images (Fig. 2).

The experimental realization of this measurement is far from obvious and different approaches to change the defocus, with different advantages and disadvantages, have been devised. For instance, the defocus might be changed by varying the specimen plane through the stage's z shift or by varying the excitation of the objective lens or some subordinate imaging lens. Typically, changing the TEM's optical system induces more changes than just a simple defocus, in particular, additional magnification changes, image rotations, distortions, and parasitic aberrations [31]. The ramifications of the latter for the 4D quantum state detected in the 2D image plane may be accounted for by the generalized transmission cross coefficient [50],

$$\rho_{\mathrm{img}}(\mathbf{x},\mathbf{x}') = \frac{1}{4\pi^2}\int d^2k d^2k' \rho(\mathbf{k},\mathbf{k}') \times \mathcal{T}(\mathbf{k},\mathbf{k}',\mathbf{x}-\mathbf{x}')e^{i(\mathbf{k}\mathbf{x}-\mathbf{k}'\mathbf{x}')}, \tag{20}$$

in the case of the most important isoplanatic aberrations. Note that each of the boldface vectors indicates a 2D coordinate. The modulations of the quantum state induced by nonisoplanatic or higher order chromatic aberrations require more elaborate computations, which are currently under development [51].

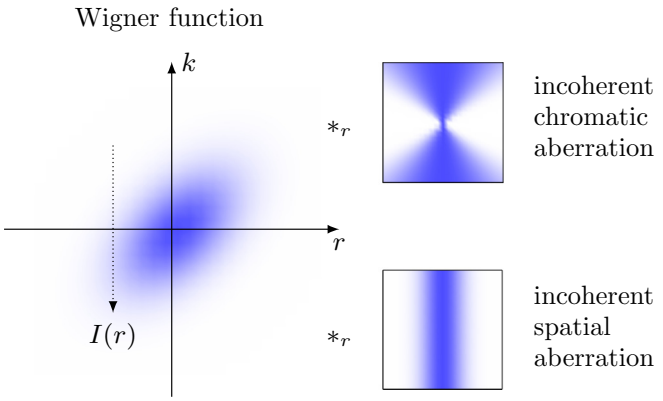

FIG. 3. (Color online) Combined effect of partial spatial and chromatic incoherence in combination with defocus and chromatic aberration (see Ref. [51] for details) on the average quantum state (i.e., with mean energy and lateral momentum). Spatial incoherence in combination with a defocus leads to a momentum-invariant convolution, which therefore may be deconvolved from the recorded image. Chromatic incoherence acts as a momentum-dependent convolution, which therefore cannot be deconvolved from a single measurement.

A great many of these unwanted side effects may be removed by a combination of hardware aberration correctors and image processing procedures [31]. For instance, the influence of varying spatial coherence on changing the defocus on a hardware-corrected TEM may be deconvolved from the recorded intensity to some extent ([31]; see Fig. 3). In the following we assume that the defocus can be adjusted perfectly in the experiments by employing these methods. We, furthermore, restrict ourselves to the paraxial regime, mostly valid for the propagation of fast electrons within the TEM.

The free-space dynamics of the Wigner function in the paraxial regime is governed by the free-space Liouville equation,

$$\left(\partial_z + \frac{1}{k_0}\mathbf{k}\cdot\nabla\right)W(\mathbf{r},\mathbf{k},z) = 0. \tag{21}$$

Accordingly, the Wigner function of a freely propagating quantum state (i.e., the solution of the above equation) reads [51,52]

$$W(\mathbf{r},\mathbf{k},z) = W\left(\mathbf{r} - \frac{z}{k_0}\mathbf{k},\mathbf{k},0\right). \tag{22}$$

Note that this is a shear in 4D phase space. Owing to this relation, an isotropic defocus series corresponds to a projection shear series in 4D phase space (see Fig. 4):

$$\rho(\mathbf{r},z) = \int W(\mathbf{r},\mathbf{k},z)\,\mathrm{d}^2k = \int W\left(\mathbf{r} - \frac{z}{k_0}\mathbf{k},\mathbf{k}\right)\mathrm{d}^2k. \tag{23}$$

The objective of phase-space tomography is to retrieve the original phase-space distribution, thereby effectively inverting the projection. There is a close relationship between the above shear series and a tomographic tilt series (see Appendix A). After inserting the dimensionless phase-space coordinates

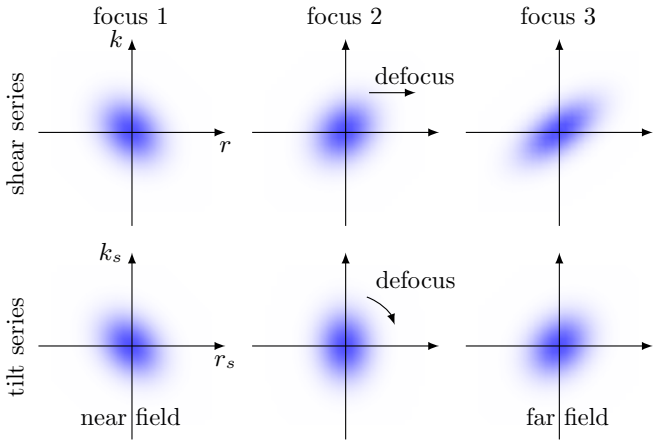

FIG. 4. (Color online) In-line holography as quantum-state reconstruction. The shear series of the defocused Wigner function is shown in the top row. The corresponding tilt series obtained by suitably scaling the phase space, (24), is depicted in the bottom row.

(scaling factor k_σ)

$$\mathbf{k}^s = \frac{k_\sigma^{-1}\mathbf{k}}{\cos\alpha} - k_\sigma \mathbf{r}\sin\alpha \quad \text{and} \quad \mathbf{r}^s = k_\sigma \mathbf{r}\cos\alpha \tag{24}$$

in the above shear series, one obtains (see Appendix A for details) the tilt series

$$\rho^s = \int W\big(k_\sigma^{-1}(\mathbf{r}^s\cos\alpha - \mathbf{k}^s\sin\alpha), k_\sigma(\mathbf{k}^s\cos\alpha + \mathbf{r}^s\sin\alpha)\big)\,\mathrm{d}^2k^s, \tag{25}$$

with

$$\rho^s = k_\sigma^{-2}\frac{\rho\left(k_\sigma^{-1}\mathbf{r}^s\cos^{-1}\alpha, z\right)}{\cos^2\alpha}. \tag{26}$$

The following points are important for the tilt-series formulation of the defocus series. First, it turns out that the tilt angle α is equal to the arctan of the inverse Fresnel number,

$$F = k_0/\left(zk_\sigma^2\right). \tag{27}$$

The latter serves as a measure to distinguish between the near-field ($F \gg 1$) and the far-field ($F \ll 1$) regimes of propagation of pure states with phase-space extensions $k_\sigma \sim r_\sigma^{-1}$ related by the uncertainty principle. Accordingly, the rotation angle α is below (above) $\pi/2$ in the near (far) field and both should be covered in order to obtain a tilt series over a tilt interval of $[0,\pi[$ required for a complete tomographic reconstruction [53]. In particular, it is generally insufficient to provide one image plane and one far-field distribution to uniquely reconstruct the quantum state, in response to Pauli's old question whether the amplitude of a function and the amplitude of its Fourier transform are sufficient to determine that function up to a constant phase [54]. Second, the intensity in (26) is scaled with $\cos^2\alpha$, which balances the growing spatial extension of the defocused quantum state. Third, the tilt series lives in 4D phase space, that is, each individual defocused image is obtained by projecting along a 2D plane in phase space tilted with the defocus. Such a projection transformation represents a generalization of the 2D Radon transformation, referred to as the K-plane transform K_2^4 in the literature (e.g., [55]), if the

set of projections is performed over all 2D planes in 4D phase space. As a consequence of the isotropic defocus, however, only a subset of projections, i.e., a restricted K-plane transform K^4_{2r}, is obtained from a defocus series,

$$k_\sigma^{-2}\frac{\rho(\cos^{-1}\alpha\mathbf{r},z)}{\cos^2\alpha} = K^4_{2r}\{W\}. \tag{28}$$

This transformation is generally not invertible if the phase-space distribution does not possess additional symmetries. This restriction can be lifted if astigmatic defoci are sampled as well, thereby realizing arbitrary shears in 4D phase space. The complexity of the projection set is the same as for the related off-axis reconstruction synthesizing phase space from slices in the 4D density matrix representation (see next section). To date, the experimental realization of the complete K-plane transform remains too complicated, and we focus in the following on simpler cases, where the phase-space distribution contains additional symmetries, allowing for a reduction of complexity.

We now consider the case where the in-focus intensity depends on only one spatial coordinate (x without loss of generality), i.e.,

$$W(\mathbf{r},\mathbf{k}) = W(x,\mathbf{k}). \tag{29}$$

This symmetry allows for a reduction of the original 4D problem to 2D in the following way. Performing the same coordinate transformation as above one obtains the familiar 2D Radon transformation,

$$k_\sigma^{-1}\frac{\rho\left(k_\sigma^{-1}\cos^{-1}\alpha x,z\right)}{\cos\alpha} = \mathcal{R}\left\{\overline{W}\left(x^s,k_x^s\right)\right\}, \tag{30}$$

relating the reduced Wigner function

$$\overline{W}(x,k_x) = \int W(x,\mathbf{k})\mathrm{d}k_y \tag{31}$$

with its defocused projections. As a consequence of the missing y dependency the reduced Wigner function can be evaluated in terms of a 2D phase space spanned by x and k_x. Note that the average of an arbitrary Wigner function in the y direction can be reconstructed along the same lines, yielding a reduced Wigner function corresponding to a projection of the original one along y and k_y.

According to the Fourier slice theorem [53], the projections of the tilted Wigner function in (30) correspond to zero sections of the Fourier-transformed tilted Wigner function: the tilted ambiguity function. Consequently, the latter may be tomographically reconstructed by appropriately assembling the sections over an azimuthal interval covering $[0,\pi[$, which can be done by tomographic reconstruction algorithms such as filtered backprojection and algebraic reconstruction algorithms [56]. The corresponding phase-space diagram of the in-line phase-space reconstruction principle is depicted in Fig. 4.

B. Off-axis electron holography

Off-axis electron holography employs an electron biprism [57] in front of an intermediary image plane to deflect the two half-planes of the quantum state towards each other (Fig. 5).

As a consequence, they superimpose farther below at the image plane forming the following quantum state [45,50] in

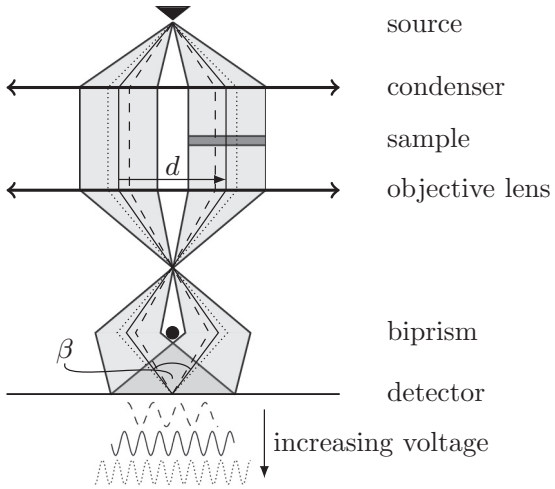

FIG. 5. Simplified optical setup for off-axis electron holography incorporating three holographic shifts dependent on the biprism voltage.

position-space density-matrix representation,

$$\begin{aligned}\rho_{\mathrm{img}}(\mathbf{x},\mathbf{x}') = {}& \rho_{++}\left(\mathbf{x}+\frac{\mathbf{d}}{2},\mathbf{x}'+\frac{\mathbf{d}}{2}\right)e^{-i\frac{\mathbf{q}_c}{2}(\mathbf{x}-\mathbf{x}')}\\ &+\rho_{--}\left(\mathbf{x}-\frac{\mathbf{d}}{2},\mathbf{x}'-\frac{\mathbf{d}}{2}\right)e^{i\frac{\mathbf{q}_c}{2}(\mathbf{x}-\mathbf{x}')}\\ &+\rho_{+-}\left(\mathbf{x}+\frac{\mathbf{d}}{2},\mathbf{x}'-\frac{\mathbf{d}}{2}\right)e^{-i\frac{\mathbf{q}_c}{2}(\mathbf{x}+\mathbf{x}')}\\ &+\rho_{-+}\left(\mathbf{x}-\frac{\mathbf{d}}{2},\mathbf{x}'+\frac{\mathbf{d}}{2}\right)e^{i\frac{\mathbf{q}_c}{2}(\mathbf{x}+\mathbf{x}')},\end{aligned} \tag{32}$$

where the hologram carrier frequency $\mathbf{q}_c = k_0\beta$ and the holographic shift $\mathbf{d}$ are indicated in Fig. 5. The first two terms correspond to the centerband (cb) and the remaining terms to the sidebands (sb), forming the interference fringes. The different electron optical transfer properties of the density matrix components require us to discriminate these expressions, e.g., with $\pm\pm$ subscripts. Note that all terms depend on the quantum state, but only the sideband terms are suitable for quantum-state reconstructions as shown below. For the sake of simplicity, we neglect Fresnel diffraction and shadowing effects at the biprism and obtain for the interference terms

$$\begin{aligned}\rho_{+-}(\mathbf{x},\mathbf{x}') &= \rho^*_{-+}(\mathbf{x},\mathbf{x}')\\ &= \int \mathrm{d}^2k\mathrm{d}^2k'\rho(\mathbf{k},\mathbf{k}')\mathcal{T}(\mathbf{k},\mathbf{k}',\mathbf{d})e^{i(\mathbf{k}\mathbf{x}-\mathbf{k}'\mathbf{x}')},\end{aligned} \tag{33}$$

where we employ the recently introduced notion of a generalized 6D holographic transmission cross coefficient [including the well-known transmission cross coefficient as $\mathcal{T}(\mathbf{k},\mathbf{k}',0)$] [50]. The interference pattern (the hologram) is simply $\rho_{\mathrm{img}}(\mathbf{x},\mathbf{x}'=\mathbf{x})$.

The hologram's Fourier spectrum can be represented by the $\mathbf{p}=0$ section of the ambiguity function, (13):

$$\begin{aligned}\tilde{W}_{\mathrm{img}}(\mathbf{q},\mathbf{p}) = {}& \tilde{W}_{++}(\mathbf{q},\mathbf{p})e^{\frac{i}{2}(\mathbf{q}\mathbf{d}+\mathbf{p}\mathbf{q}_c)} + \tilde{W}_{--}(\mathbf{q},\mathbf{p})e^{-\frac{i}{2}(\mathbf{q}\mathbf{d}+\mathbf{p}\mathbf{q}_c)}\\ &+\tilde{W}_{+-}(\mathbf{q}+\mathbf{q}_c,\mathbf{p}+\mathbf{d}) + \tilde{W}_{-+}(\mathbf{q}-\mathbf{q}_c,\mathbf{p}-\mathbf{d}).\end{aligned} \tag{34}$$

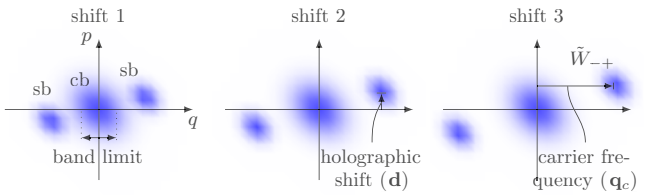

FIG. 6. (Color online) Quantum-state [ambiguity function; Eq. (34)] reconstruction by off-axis holography measuring the cross section $\tilde{W}_{-+}(\mathbf{q},\mathbf{p}=0)$ of the sideband (sb) for different holographic shifts ($\mathbf{d}$). A sufficiently high carrier frequency ($\mathbf{q}_c$) permits separation between centerbands (cb) and sidebands.

Consequently, the real-space interference term intensity may be separated by numerically applying a filter in reciprocal space, if the phase-space distribution obeys some band limit, i.e., $\tilde{W}(\mathbf{q},\mathbf{p})=0$ for $|\mathbf{q}|>q_B$.

The ambiguity function immediately reveals the working principle of a quantum-state reconstruction by means of off-axis holography (Fig. 6). By changing the holographic shear $\mathbf{d}$ (biprism voltage), different sections of the (sideband) ambiguity function are shifted to $\mathbf{p}=0$, eventually facilitating a tomographic reconstruction of the complete quantum state. Note that the centerband terms $\tilde{W}_{\pm\pm}$ do not vary with the biprism voltage and, hence, are not suited for a quantum-state reconstruction. The ambiguity function in the $\mathbf{p}$ direction returns the lateral coherence at the image plane dependent on the holographic shear $\mathbf{d}$. This implies that for a given spatial coherence the interference term will strongly attenuate for shears larger than the width of coherence. The measurement of spatial coherence dependent on the shear returns the conventionally inaccessible off-diagonals.

Note that covering the whole range of $\mathbf{d}$ requires varying the biprism voltage as well as both its orientation and its position. To date, no complete quantum-state reconstruction by off-axis holography has been reported. However, the complexity of the method may be significantly reduced in the presence of additional symmetries. In the case of homogeneous objects $[\rho(\mathbf{k},\mathbf{k}')=\rho(\mathbf{k})\delta(\mathbf{k}-\mathbf{k}')]$ the interference term, (33), depends only on the relative distances and the influence of partial coherent illumination factorizes $[\mathcal{T}(\mathbf{q},\mathbf{q},\mathbf{d})=\mathcal{T}(\mathbf{0},\mathbf{0},\mathbf{d})]$:

$$\rho_{+-}(\mathbf{r}-\mathbf{r}')=\mathcal{T}(0,0,\mathbf{d})\rho(\mathbf{r}-\mathbf{r}'). \tag{35}$$

For objects being homogeneous only in the normal direction of the biprism (e.g., plane surfaces), 1D cuts of the density matrix can be reconstructed dependent on the distances to them [45,50,58–60].

C. Differential phase contrast

DPC in its literal sense, i.e., as a phase (and therefore wave) reconstruction method, can be obtained with various optical setups, with the most prominent ones in transmission electron microscopy being the so-called transport of intensity equation (TIE) reconstruction [16,33,61] and the scanning transmission electron microscopy (STEM)-DPC setup [32,34,44]. The TIE setup, depicted in Fig. 7, is a bright-field mode, whereas STEM-DPC is a scanning transmission electron microscopy technique utilizing the scanning point as a degree of freedom.

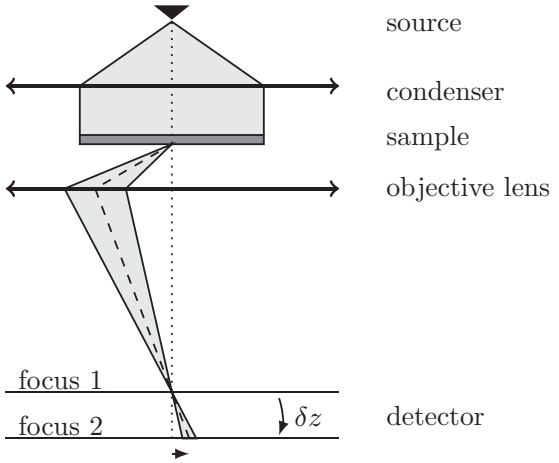

FIG. 7. Astigmatic TIE setup in one lateral dimension. The defocus step is denoted δz. The differential shift of the intensity with respect to the neighboring image point is indicated by the arrow.

Although the two modes have a lot in common, in particular, when considering the above-noted axial scattering approximation, we discuss them separately because of the following. The bright-field mode can be extended to a quantum-state reconstruction of the electron beam similar to the previously discussed off-axis and inline holography. Contrary to that, the STEM-DPC setup does not permit a quantum-state reconstruction of the electron beam itself. However, within the scope of single axial scattering, it makes for an elegant and experimentally simple reconstruction of the phase-space representation of the generalized object transparency, referred to as ptychography. This distinction, with respect to the object to be reconstructed, is also crucial when discussing superresolution techniques and we return to this point below. In the conventional TIE setup (Fig. 7), one records two slightly defocused images in the near field to approximate the left-hand side of the TIE (i.e., the paraxial continuity equation)

$$\frac{\partial\rho(\mathbf{r})}{\partial z}=-\frac{1}{k_0}\nabla\cdot\mathbf{j}(\mathbf{r}), \tag{36}$$

which may then be solved for the conservative (curl-free) part of the current density provided that appropriate boundary conditions are given [16,62]. The complete current density may be obtained by separately applying two perpendicular astigmatic defoci along x and y and solving [44]

$$(\partial_z\rho(\mathbf{r}))_{x,y}=-\frac{1}{k_0}\partial_{x,y}j_{x,y} \tag{37}$$

to obtain

$$j_{x,y}(\mathbf{r})=-k_0\int(\partial_z\rho(\mathbf{r}))_{x,y}\mathrm{d}x,y+j_{0x,y}. \tag{38}$$

In contrast to in-line holography and off-axis holography the TIE has not been considered as quantum-state reconstruction before. However, the phase-space interpretation of the above lines suggests the following extension. According to (7), the conventional TIE reconstruction yields the zeroth- and first-order generalized probability current. Consequently, the complete quantum state may be obtained if all (or a sufficiently

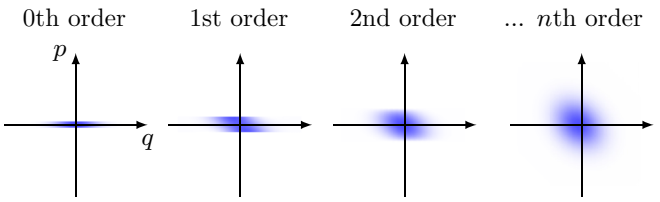

FIG. 8. (Color online) Generalized TIE as quantum-state reconstruction. Moments with increasing order correspond to a Taylor expansion of the ambiguity function.

large number) of the generalized currents and therefore moments of the Wigner function can be reconstructed. Since the moments of the Wigner function correspond to the derivatives of the ambiguity function (along p at $p = 0$), a given number of moments can be used to approximate the ambiguity function, (8), as a Taylor series (Fig. 8).

In order to measure (at least some) higher order generalized currents, we propose the following two procedures: first, an evaluation of higher order differentials of the intensity with respect to the defocus and, second, the evaluation of intensity differentials with respect to higher order isoplanatic aberrations. The latter became possible with the advent of modern hardware aberration correctors capable of tuning aberrations up to the fourth order. To illustrate both working principles, we note the corresponding expression for the second-order generalized currents $j^{(2)}_{xx}$ (see Appendix B for details). In the first case, the z derivative of the (first-order) probability current corresponds to the spatial derivative of the second-order current according to

$$\partial_z j^{(1)}_x(\mathbf{r}) = -\frac{1}{k_0}\partial_x j^{(2)}_{xx}(\mathbf{r}). \tag{39}$$

Indeed, there is a complete hierarchy of identical equations relating the nth-order current to the $(n+1)$th order [63]:

$$\partial_z j^{(n)}_{n\times x}(\mathbf{r}) = -\frac{1}{k_0}\partial_x j^{(n+1)}_{(n+1)\times x}(\mathbf{r}). \tag{40}$$

In the second case we record two images with a slight change of the x component of the second-order isoplanatic aberrations C_{20} (i.e., a combination of axial coma and threefold astigmatism; see Appendix B for details), yielding the differential equation

$$\partial_{C_{20}}\rho^*(\mathbf{r}) = -\frac{1}{k_0^2}\partial_x j_{xx}, \tag{41}$$

with

$$\rho^*(\mathbf{r}) = \mathcal{F}^{-1}\left\{\mathcal{F}\{\rho(\mathbf{r})\}e^{\frac{i}{12}C_{20}q_x^3}\right\}. \tag{42}$$

As noted, such a measurement has not been conducted in the TEM to date. Similarly to the above two methods (off-axis and in-line), the experimental effort is challenging and it is certainly expedient to begin again with 1D objects when exploring this hitherto pristine field.

D. Ptychography

As discussed in the previous section there is an alternative DPC setup utilizing the scanning mode of the TEM. Here, the center of mass in momentum space is measured by placing a suitable detector in the far field of the specimen plane (Fig. 9).

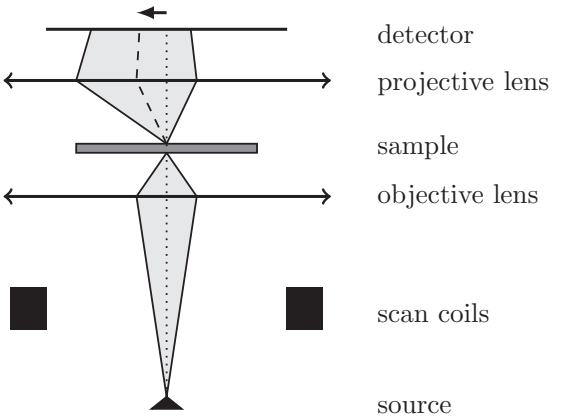

FIG. 9. STEM-DPC setup in one lateral dimension. The shift of the momentum's barycenter recorded in the far field of the specimen is indicated by the arrow.

The corresponding DPC signal for one scanning point reads [44]

$$\mathbf{s} = \int \mathbf{j}(\mathbf{r})\mathrm{d}^2 r. \tag{43}$$

By employing a pixel detector, spatially sampling the far-field intensity distribution, it is straightforward to obtain an integral value of the generalized currents according to

$$\mathbf{s}^{(n)} = \int \mathbf{j}^{(n)}(\mathbf{r})\mathrm{d}^2 r. \tag{44}$$

However, the STEM-DPC setup is not designed to determine the quantum state of the scattered electron beam since only a single intensity measurement per scan point (without superimposing with a known reference) is performed.

Instead, the STEM setup turns out to facilitate a simple and efficient reconstruction of the mutual object transparency within the scope of the single axial scattering approximation. The basic idea is to utilize the incoming quantum state of the STEM beam as an invariant probe for the object transparency facilitating a direct reconstruction of the latter without taking a detour over the scattered beam quantum state as done by the above-discussed methods. The following lines illustrate the working principle [64]. Employing the bra-ket notation, we start by writing the far-field intensity in the axial approximation,

$$\begin{aligned} I(k) &= \int \mathrm{d}x\mathrm{d}x'\langle k|x\rangle\langle x|\hat{\rho}_f|x'\rangle\langle x'|k\rangle \\ &= \frac{1}{2\pi}\int \mathrm{d}x\mathrm{d}x'\, e^{-ikx}T(x,x')\rho_i(x-x_i,x'-x_i)e^{ikx'}, \end{aligned} \tag{45}$$

where x_i denotes the probe position. Inserting the Wigner transform of the mutual object transparency and the probe state into (45), one obtains an alternative expression of the reciprocal-space intensity at a particular probe position in terms of Wigner transforms (functions),

$$I(r_i,k_p) = \int \mathrm{d}r\mathrm{d}k\, T_W(r,k)W_i(r-r_i,k_p-k). \tag{46}$$

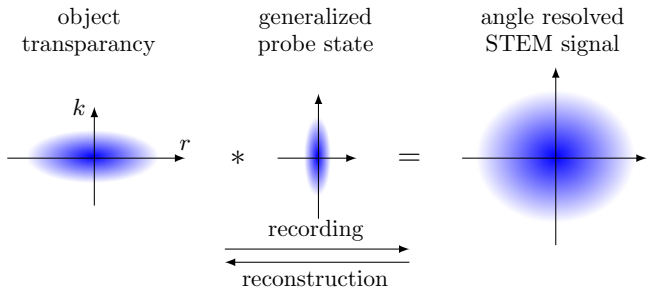

FIG. 10. (Color online) Ptychography as (de)convolution of the Wigner transformed axial scattering operator. Accordingly, the smaller (i.e., purer) the probe's Wigner function phase-space volume, the larger the corresponding low pass truncating the corresponding ambiguity function of the axial scattering operator (Fourier transform of the Wigner transform).

Consequently, the complete set of measured intensities dependent on the probe position r_i and scattering momentum k_p,

$$I(r,k) = T_W(r,k) * W_i(-r,k), \tag{47}$$

corresponds to a convolution of the transparency's and the probe's Wigner transforms in phase space (Fig. 10), which corresponds to a multiplication of ambiguity functions in reciprocal phase space,

$$\tilde{I}(q,p) = -\tilde{T}_W(q,p)\tilde{W}_i(-q,p). \tag{48}$$

Ptychography refers to the technique seeking an inversion (deconvolution) of the phase-space convolution. Several deconvolution strategies, eventually incorporating additional constraints, have been developed to date. The original approach, referred to as the Wigner distribution deconvolution method (WDDM), consists of using (regularized) deconvolution algorithms in combination with separately determined probe quantum states [64–66]. Typically, the deconvolution is limited at the zeros of the probe's ambiguity function, defining a (band) limit for the quantum-state reconstruction (see Fig. 10). Consequently, a strictly positive probe's ambiguity function with an extension as large as possible, that is, a (squeezed) coherent state ($\zeta = 1$), provides the optimal probe function for this type of reconstruction [67]. Therefore, ptychography in the TEM may greatly profit from advanced electron sources, taking into account that current field emission electron guns, at best, provide purities [68] in the range of 10^{-2} to 10^{-3} [51]. The second important experimental parameter occurring in the convolution, (46), is the extension of the detector in momentum space (the k_p boundaries), which should be large enough to facilitate a complete sampling of the object transparency's Wigner function (see Fig. 10).

In response to the large computational costs of a deconvolution in 4D phase space, iterative reconstruction methods (e.g., the ptychographic iterative engine) [69]) incorporating additional constraints on both the purity of the probe quantum state and the mutual object transparency have been devised. Owing to the required purity the phase-space deconvolution may be performed in the wave-function representation, cutting the dimensionality of the problem in half. It has been shown that these iterative approaches even facilitate a concomitant reconstruction of the probe's wave function [70,71], although the mathematical rigorous foundations behind such a blind deconvolution still remain somewhat in the dark. Recently, the more general scope of the WDDM, allowing for treating general mixed quantum states, has been recognized and exploited to improve x-ray ptychographic reconstructions [72]. Note, however, that the validity of the single axial scattering approximation is severely limited to certain imaging regimes for fast electrons in the TEM (see Sec. II). This particularly pertains to atomic resolution, where dynamic scattering effects eventually invalidate the ptychographic reconstruction principle.

IV. COMPARISON

Based on our above phase-space considerations we may now set out to compare the different forms of electron holography and their perspective for phase-space reconstruction. First, we have noted that a variety of experimental limitations imposed by the electron optics employed in current TEMs prevents a complete reconstruction of a general 4D quantum state no matter what holographic scheme is used. Quantum-state tomography based on in-line holography requires the ability to set any line defocus between near and far field with a varying orientation. In particular, the requirement of a complete defocus range ranging from the near to the far field seems to be unrealistic for current stigmators based on weak quadrupoles. Off-axis holography employing rotatable biprisms facilitates the recording of a sufficient number of phase-space sections required for a reconstruction. However, the varying aberrations and the beam shaping influence of the biprism, such as shadowing and Fresnel scattering, seriously complicate the reconstruction. The latter effect may be accounted for in the quantum-state reconstruction in the case of small angle diffraction [50] or largely suppressed by advanced multiple biprism setups [19,73]. Finally, the generalized TIE requires only a differential change of line defoci, which can be accomplished by modern TEM stigmators. However, the analyzable number of momentum moments is severely limited here. Ptychography elegantly circumvents all these issues by reconstructing a generalized object transparency instead of the quantum state of the scattered electrons. This obviously requires the single axial scattering approximation to be valid, which seriously limits the use of ptychography in the atomic-resolution domain, where dynamic scattering effects become significant [74].

Until the above limitations have been overcome, the results of a quantum-state reconstruction depend on the optimal choice of the holographic method or combinations thereof. For instance, ptychography seems to be optimal within the scope of single axial scattering. The generalized TIE may be used if only the first three generalized currents, i.e., the density, the probability current, and the momentum variance, are required. Off-axis holography is well suited for the study of coherence at comparatively large lengths in a quantum state, and in-line holography may be applied to quantum states of particular symmetry, in particular, 1D systems.

The phase-space perspective, furthermore, allows for discussion of the respective requirements for a successful wave reconstruction, i.e., the conventional scope of electron

holography, because of the following (see [22] for a discussion of x-ray holography). According to (1) and (4) the wave completely defines the phase-space distribution, and conventional holography may be considered as a phase-space reconstruction of a pure state (a wave). In other words, wave reconstruction holography is a phase-space reconstruction under the two constraints that the purity, (8), strictly equals 1 ($\zeta = 1$) and the Wigner function is bounded ($|W(\mathbf{r},\mathbf{k})| \leqslant 1/\pi$ [75]). Given the infinitely large space of allowed quantum states, such constraints only marginally restrict the reconstruction domain. Consequently, existence and uniqueness theorems for quantum-state reconstructions may be transferred to wave reconstructions [21,76]. In the case of the in-line scheme a detailed study of the uniqueness of the phase retrieval problem has been reported by Jaming [76], who reveals which additional constraints on the reconstruction domain, such as finite support and particular basis functions, are suited to reduce the focal range required for a unique reconstruction. These investigations are very helpful for characterizing the outcome of the widely employed Gerchberg-Saxton-type iterative in-line reconstruction schemes [77,78]. Indeed, these iterative in-line reconstruction schemes typically employ such additional *a priori* information, constraining, for instance, the wave function's support, topology, or smoothness, in order to obtain sufficiently unique results. Off-axis holography takes a completely different route to ensure uniqueness by using a known (typically flat) reference wave, providing a one-to-one relationship between the interference pattern and the reconstructed wave if the latter obeys a certain spatial band limit (see Sec. III B).

To take into account partial coherence, wave reconstructions typically model the ramifications of the mixed state for the observed intensity distribution in the hope of obtaining a sufficiently unique wave reconstruction. From a phase-space perspective this amounts to taking into account a modification (typically a blurring) of the phase space (see, e.g., Fig. 3) in the pure-state reconstruction scheme. Inverting the latter prior to reconstruction typically invokes some ill-conditioned procedure such as the deconvolution of the spatial and temporal envelope in off-axis holography or the deconvolution of spatial incoherence in the spherical aberration corrected instrument (Fig. 3). Consequently, the scope of wave reconstructions from incoherent or mixed states is limited even if the mixing process is well known.

We close this section with a short and incomplete discussion of enhanced resolution or superresolution, referring to techniques seeking to overcome the resolution limits in the acquired micrograph due to the phase-space blurring introduced by incoherent aberrations (e.g., Fig. 3) [79]. From a phase-space perspective one may define the spatial resolution as the band limit of the quantum state's ambiguity function at $p = 0$ along q corresponding to the experimental diffractogram [Eq. (13)]. This measure of spatial resolution has to be distinguished from the extension of the Wigner distribution along the momentum axis (i.e., the size of the experimental Fourier spectrum) as, for a general mixed (partially coherent) quantum state, those two measures may be completely independent. A special case of the latter observation is the well-known fact that the size of the Fourier transform of the intensity (i.e., the diffractogram) of a wave is usually larger than that of the Fourier spectrum of the wave, as the former corresponds to the autocorrelation of the wave's Fourier transform. Nevertheless, one frequently encounters superresolution measures based on comparing those two, e.g., by evaluating data taken at the diffraction plane and the image plane (or comparing linear imaging resolution with nonlinear resolution [80]). Such a comparison is only well defined if a connection between these extensions can be established, e.g., by *a priori* assuming or attaining knowledge of the electron's wave function within the superresolution setup. Indeed, a large class of superresolution schemes is holographic in nature, in that they seek a reconstruction of a wave function or a complex transmission function with superresolution, by removing the influence of the aberrations. Here, examples of *a priori* knowledge are the elastic single axial scattering assumption employed in ptychography (see above) and the support constraints often used in diffractive imaging superresolution schemes. Nevertheless, the numerical inversion of the phase-space convolution due to aberrations will be effectively limited. Thus, a set of multiple holographic reconstructions with different blurring such as proposed in Ref. [81] could provide a valuable alternative to the established superresolution methods.

V. SUMMARY

In summary, we exhibit a phase-space perspective on the most popular phase retrieval or holographic techniques currently employed in the TEM, namely, off-axis and in-line holography as well as DPC and ptychography. We give explicit phase-space expressions including the important aberrations and phase-space diagrams of the corresponding holographic principles. Based on these findings we discuss the important characteristics of conventional wave reconstruction as well as the extensions of electron holography towards quantum-state reconstruction. To that end, we exhibit the pertinent reconstruction strategies and discuss the current experimental limitations.

The main goal of the above considerations is an extension of electron holography towards characterizing incoherent electron scattering, in particular, inelastic scattering. Currently, only a small number of such investigations have been conducted, almost exclusively with the off-axis setup. Due to the restricted shift distance, however, the obtained results have been limited mainly to an experimental verification of long-range Coulomb interactions. Our results show that ptychography and the generalized TIE are not limited in that respect. Consequently, these holographic techniques commend themselves for the study of correlation effects in plasmonic excitations such as correlation hole and core-loss excitations, including the electron microscopic chiral dichroism (EMCD) [82].

A second area of application is the characterization of electron beam properties including aberrations without requiring test structures. Instead, the information is directly extracted from the reconstructed quantum state of the electron beam and its deformations. In particular, the combination of the probe's quantum-state reconstruction and ptychography as a phase-space deconvolution technique may be beneficially used in the future to study a wide range of delocalized inelastic low-loss excitations such as surface plasmons.

Last but not least, the presented quantum-state reconstructions offer new pathways towards superresolution, as the quantum state comprises the maximally obtainable information on scattered electrons. In particular, ultrafast TEM investigations employing incoherent bunches of electrons are prone to profit from the discussed reconstruction techniques, thereby increasing the resolution and information content of the recorded data. For instance, "conventional" electron holographic investigations of electric, magnetic, or strain fields in solids may be conducted with incoherent probes by applying the phase-space reconstruction principles.

ACKNOWLEDGMENTS

The authors gratefully acknowledge fruitful, critical, and inspiring discussions with Prof. Dr. H. Lichte and J. Krehl (TU Dresden, Germany). This work was supported by DIP, the German-Israeli Project Cooperation of the DFG (Germany).

APPENDIX A: IN-LINE HOLOGRAPHY AND TOMOGRAPHY

In order to establish the relation between the defocus series and the Radon transformation, we first introduce dimensionless phase-space coordinates by scaling with some (reciprocal) length scale k_σ:

$$\mathbf{k}' = k_\sigma^{-1}\mathbf{k} \quad \text{and } \mathbf{r}' = k_\sigma \mathbf{r}. \tag{A1}$$

In principle, the scaling factor may assume any value, because this has no influence on the reconstruction as detailed below. However, for numerical purposes, it is advantageous to set a value ensuring a similar extension of the quantum state in the scaled phase-space coordinates. For instance, a pure state with a characteristic momentum width Δk has a position width $\Delta r = \Delta k^{-1}$, which leads to a round distribution in scaled phase space if the scaling factor is set to $k_\sigma = \Delta k$. In scaled phase-space coordinates the defocused intensity can be written as

$$\rho\left(k_\sigma^{-1}\mathbf{r}',z\right) = k_\sigma^2 \int W\left(k_\sigma^{-1}\left(\mathbf{r}' - \underbrace{\frac{zk_\sigma^2}{k_0}}_{\tan\alpha}\mathbf{k}'\right), k_\sigma \mathbf{k}'\right) \mathrm{d}^2k', \tag{A2}$$

where we have introduced an angular representation for the shear simplifying the following notation. We now seek a coordinate transformation transforming the shear into a rotation of phase space according to

$$\rho\left(k_\sigma^{-1}\mathbf{r}'(\mathbf{r}^s,\mathbf{k}^s),z\right) = k_\sigma^2 \cos^2\alpha \int W\left(k_\sigma^{-1}(\mathbf{r}^s\cos\alpha - \mathbf{k}^s\sin\alpha), k_\sigma(\mathbf{k}^s\cos\alpha + \mathbf{r}^s\sin\alpha)\right)\mathrm{d}^2k^s. \tag{A3}$$

The corresponding transformation pair reads

$$\mathbf{k}' = \mathbf{k}^s\cos\alpha + \mathbf{r}^s\sin\alpha \quad \text{and } \mathbf{r}' = \frac{\mathbf{r}^s}{\cos\alpha}, \tag{A4}$$

$$\mathbf{k}^s = \frac{\mathbf{k}'}{\cos\alpha} - \mathbf{r}'\sin\alpha \quad \text{and } \mathbf{r}^s = \mathbf{r}'\cos\alpha, \tag{A5}$$

yielding

$$k_\sigma^{-2}\frac{\rho\left(k_\sigma^{-1}\cos^{-1}\alpha\mathbf{r}_\perp^s,z\right)}{\cos^2\alpha} = \int W\left(k_\sigma^{-1}(\mathbf{r}^s\cos\alpha - \mathbf{k}^s\sin\alpha), k_\sigma(\mathbf{k}^s\cos\alpha + \mathbf{r}^s\sin\alpha)\right)\mathrm{d}^2k^s. \tag{A6}$$

Consequently, the shear series may be treated as a tilt series,

$$\rho^s = k_\sigma^{-2}\frac{\rho\left(k_\sigma^{-1}\mathbf{r}^s\cos^{-1}\alpha,z\right)}{\cos^2\alpha}, \tag{A7}$$

that is, a restricted K-plane transform K_{2r}^4,

$$\rho^s = K_{2r}^4\{W(\mathbf{r}^s,\mathbf{k}^s)\}. \tag{A8}$$

APPENDIX B: DIFFERENTIAL PHASE CONTRAST AND ISOPLANATIC ABERRATIONS

In the first proposed method, nth-order moments of the Wigner function (generalized currents) are derived from astigmatic differential defoci of $(n-1)$th-order moments. In the following we derive the corresponding equation forming the basis of the reconstruction of the second-order generalized currents. Here, the use of line defoci permits the usage of the free-space 1D Liouville equation. We compute the line defocus derivative along x by inserting the definition of the current in the first line and the free-space 1D Liouville equation in the second line of the following equation to obtain

$$\begin{aligned}\partial_z j_x(\mathbf{r}) &= \partial_z \int k_x W(\mathbf{r},\mathbf{k})\mathrm{d}^2k \\ &= -\int \frac{k_x}{k_0}k_x\partial_x W(\mathbf{r},\mathbf{k})\mathrm{d}^2k = -\frac{1}{k_0}\partial_x j_{xx}^{(2)}(\mathbf{r}).\end{aligned} \tag{B1}$$

Other directional components, such as $j_{xy}^{(2)}$ and higher order moments, may be derived along corresponding lines. The realization of the above reconstruction principle requires minute control of line defoci, which is complicated, in particular, in the high-resolution domain. Current TEM instrumentation allows very precise control of the isotropic defocus instead. Similarly to the restriction of the current reconstruction to conservative currents, one obtains certain subinformation on second-order currents in this case. To derive the corresponding reconstruction principle, we first note the isotropic defocus differential of the current,

$$\begin{aligned}\partial_z\mathbf{j}(\mathbf{r}) &= \partial_z\int \mathbf{k}W(\mathbf{r},\mathbf{k})\mathrm{d}^2k = -\int\frac{\mathbf{k}}{k_0}\mathbf{k}\cdot\nabla W(\mathbf{r},\mathbf{k})\mathrm{d}^2k \\ &= -\frac{1}{k_0}\begin{pmatrix}\partial_x j_{xx}^{(2)}(\mathbf{r}) + \partial_y j_{xy}^{(2)}(\mathbf{r}) \\ \partial_x j_{xy}^{(2)}(\mathbf{r}) + \partial_y j_{yy}^{(2)}(\mathbf{r})\end{pmatrix}.\end{aligned} \tag{B2}$$

We now use this result to compute the second-order derivative of the intensity with respect to an isotropic defocus:

$$\begin{aligned}\partial_{zz}\rho(\mathbf{r}) &\overset{(36)}{=} -\frac{1}{k_0}\partial_z\nabla\cdot\mathbf{j}(\mathbf{r}) = -\frac{1}{k_0}\nabla\cdot\partial_z\mathbf{j}(\mathbf{r}) \\ &\overset{(B2)}{=} \frac{1}{k_0^2}\nabla\cdot\begin{pmatrix}\partial_x j_{xx}^{(2)}(\mathbf{r}) + \partial_y j_{xy}^{(2)}(\mathbf{r}) \\ \partial_x j_{xy}^{(2)}(\mathbf{r}) + \partial_y j_{yy}^{(2)}(\mathbf{r})\end{pmatrix} \\ &= \frac{1}{k_0^2}\left(\partial_{xx} j_{xx}^{(2)}(\mathbf{r}) + 2\partial_{xy} j_{xy}^{(2)}(\mathbf{r}) + \partial_{yy} j_{yy}^{(2)}(\mathbf{r})\right).\end{aligned} \tag{B3}$$

This equation cannot be integrated to some second-order current if the quantum state does not possess suitable additional symmetries (such as radial symmetry) providing additional dependencies between the different components of $j^{(2)}$.

The derivation of the constituting equation for the reconstruction of higher order moments from differentials with respect to some higher order isoplanatic aberrations is more involved. Isoplanatic aberrations in the TEM modify the object exit wave function by a multiplication of a phase plate in the back focal plane,

$$\Psi_{\mathrm{img}}(\mathbf{k}) = \Psi_{\mathrm{obj}}(\mathbf{k}) e^{-i\chi(\mathbf{k})}, \tag{B4}$$

where the different orders of aberrations correspond to the homogeneous polynomials of that order in χ (see [83] for a similar notation):

$$\chi(\mathbf{k}) = \sum_{n=1}^{\infty} \frac{1}{(n+1)k_0^n} \sum_{l=0}^{n} C_{nl} k_x^l k_y^{n-l}. \tag{B5}$$

Note that the aberration coefficient definition applied here deviates from the usual one to facilitate a partial separation into distinguished Cartesian directions. The typical polar notation for the most important first three orders reads

$$\begin{aligned}\chi(\mathbf{k}) = &\underbrace{\frac{C_1}{2k_0}|\mathbf{k}|^2}_{\text{defocus}} + \underbrace{\frac{A_1}{2k_0}|\mathbf{k}|^2\cos 2\alpha}_{\text{2-fold astigmatism}} \\ &+ \underbrace{\frac{B_2}{k_0^2}|\mathbf{k}|^3\cos\alpha}_{\text{axial coma}} + \underbrace{\frac{A_2}{3k_0^2}|\mathbf{k}|^3\cos 3\alpha}_{\text{3-fold astigmatism}} \\ &+ \underbrace{\frac{C_3}{4k^3}|\mathbf{k}|^4}_{\text{spherical aberration}} + \underbrace{\frac{A_3}{4k_0^3}|\mathbf{k}|^4\cos 4\alpha}_{\text{4-fold astigmatism}} + \underbrace{\frac{S_3}{k_0^3}|\mathbf{k}|^4\cos 2\alpha}_{\text{star aberration}},\end{aligned} \tag{B6}$$

which may be directly translated into the Cartesian notation used in the paper, (B5). We have dropped the characteristic azimuthal angles for the sake of clarity.

We again illustrate the reconstruction principle using the example of second-order currents. In contrast to the first reconstruction principle, the extension to higher order currents seems not to be straightforward and is not further elaborated here. To make further progress we note the Wigner function in the presence of second-order aberrations $\chi^{(2)}$ (denoted by the subscript img) [51]:

$$\begin{aligned}W_{\mathrm{img}}(\mathbf{r},\mathbf{k}) = &\; W(\mathbf{r} - \nabla\chi^{(2)}(\mathbf{k}),\mathbf{k}) \\ &*_r \frac{1}{4\pi^2}\int \mathrm{d}^2k' e^{-\frac{i}{4}\chi^{(2)}(\mathbf{k}')} e^{i\mathbf{k}'\mathbf{r}}.\end{aligned} \tag{B7}$$

The convolution in position space can be directly inverted by multiplying with $\exp(\frac{i}{4}\chi^{(2)}(\mathbf{k}'))$ in the Fourier transform of W_{img} along the position space, yielding

$$W^*_{\mathrm{img}}(\mathbf{r},\mathbf{k}) = W(\mathbf{r} - \nabla\chi^{(2)}(\mathbf{k}),\mathbf{k}). \tag{B8}$$

This second-order aberrated Wigner function is now very similar to the previously discussed first-order one in that only a change of the argument, i.e., a classical distortion of the phase-space distribution, is present. We can consequently proceed in exactly the same way as above, i.e., we translate the derivative of the intensity with respect to the second-order aberration coefficient along x into a corresponding derivative of the Wigner function according to

$$\begin{aligned}\partial_{C_{20}}\rho^*(\mathbf{r}) &= \int \partial_{C_{20}} W^*_{C_{20}}(\mathbf{r},\mathbf{k})\mathrm{d}^2k \\ &= \int \partial_{C_{20}} W\left(\mathbf{r} - \frac{C_{20}k_x^2}{k_0^2}\mathbf{e}_x,\mathbf{k}\right)\mathrm{d}^2k \\ &= -\int \frac{k_x^2}{k_0^2}\partial_x W\left(\mathbf{r} - \frac{C_{20}k_x^2}{k_0^2}\mathbf{e}_x,\mathbf{k}\right)\mathrm{d}^2k \\ &= -\frac{1}{k_0^2}\partial_x j_{xx},\end{aligned} \tag{B9}$$

which readily yields the second-order current. The derivatives with respect to the other second-order aberrations follow in a similar way. The complication in the case of $n > 2$ order aberrations arise because it is no longer possible to deconvolve the quantum part of the aberration from the intensity. Consequently, we may not compute ρ^*, which significantly complicates the link between the partial intensity derivatives and the higher order currents.

We finally note an interesting corollary to the above considerations. Upon slightly changing the spherical aberration we obtain the following wave function in reciprocal space,

$$\Psi(\mathbf{k},C_3) = \left(1 - i\frac{C_3}{4k^3}|\mathbf{k}|^4\right)\Psi(\mathbf{k}), \tag{B10}$$

and position space,

$$\begin{aligned}\Psi(\mathbf{r},C_3) &= \mathcal{F}^{-1}\{\Psi(\mathbf{k},C_3)\} \\ &= \left(1 - i\frac{C_3}{4k^3}\triangle^2\right)\Psi(\mathbf{r}).\end{aligned} \tag{B11}$$

As noted by Allen *et al.* [83], the differential with respect to the spherical aberration is then proportional to the biharmonic Laplace operator,

$$\begin{aligned}\frac{\partial\Psi(\mathbf{r},C_3)}{\partial C_3} &= \lim_{C_3\to 0}\frac{\Psi(\mathbf{r},C_3) - \Psi(\mathbf{r})}{C_3} \\ &= -i\frac{1}{4k^3}\triangle^2\Psi(\mathbf{r}).\end{aligned} \tag{B12}$$

We may now compare (B12) with the paraxial Schrödinger equation, yielding the following expression for the differential:

$$\frac{\partial\Psi(\mathbf{r},C_3)}{\partial C_3} = \frac{i}{4k}\frac{\partial^2\Psi(\mathbf{r})}{\partial^2 z}. \tag{B13}$$

In the final step we compute a modified TIE,

$$\begin{aligned}\frac{\partial\rho(\mathbf{r},C_3)}{\partial C_3} &= \frac{i}{4k}\left(\Psi^*(\mathbf{r})\partial_z^2\Psi(\mathbf{r}) - \Psi(\mathbf{r})\partial_z^2\Psi^*(\mathbf{r})\right) \\ &= \frac{i}{4k}\partial_z\left(\Psi^*(\mathbf{r})\partial_z\Psi(\mathbf{r}) - \Psi(\mathbf{r})\partial_z\Psi^*(\mathbf{r})\right) \\ &= -\frac{1}{4k}\partial_z j_z,\end{aligned} \tag{B14}$$

exhibiting a remarkable link to the z derivative of the paraxial current density.

[1] D. Gabor, Nature **161**, 777 (1948).
[2] O. Scherzer, Z. Phys. **101**, 593 (1936).
[3] P. Hariharan, *Basics of Holography* (Cambridge University Press, Cambridge, UK, 2002).
[4] R. P. Millane, J. Opt. Soc. Am. A **7**, 394 (1990).
[5] L. D. Marks, W. Sinkler, and E. Landree, Acta Crystallogr. Sec. A **55**, 601 (1999).
[6] A. Tonomura, T. Matsuda, J. Endo, T. Arii, and K. Mihama, Phys. Rev. Lett. **44**, 1430 (1980).
[7] P. A. Midgley and R. E. Dunin-Borkowski, Nat. Mater. **8**, 271 (2009).
[8] T. Kasama, R. E. Dunin-Borkowski, and M. Beleggia, in *Holography—Different Fields of Application*, edited by F. Monroy (InTech, http://www.intechopen.com, 2011).
[9] H. Lichte, F. Börrnert, A. Lenk, A. Lubk, F. Röder, J. Sickmann, S. Sturm, K. Vogel, and D. Wolf, Ultramicroscopy **134**, 126 (2013).
[10] J. C. Dainty and J. R. Fienup, *Image Recovery: Theory and Applications* (Academic Press, Orlando, FL, 1987), pp. 231–275.
[11] J. R. Fienup, J. C. Marron, T. J. Schulz, and J. H. Seldin, Appl. Opt. **32**, 1747 (1993).
[12] M. E. Haine and T. Mulvey, J. Opt. Soc. Am. **42**, 763 (1952).
[13] R. Collier, C. Burckhardt, and L. Lin, *Optical Holography*, student ed. (Academic Press, New York, 1971).
[14] E. Völkl, L. Allard, and D. C. Joy (eds.), *Introduction to Electron Holography* (Kluwer Academic/Plenum, New York, 1999).
[15] J. R. Fienup and C. C. Wackerman, J. Opt. Soc. Am. A **3**, 1897 (1986).
[16] A. Lubk, G. Guzzinati, F. Börrnert, and J. Verbeeck, Phys. Rev. Lett. **111**, 173902 (2013).
[17] A. Tonomura, N. Osakabe, T. Matsuda, T. Kawasaki, J. Endo, S. Yano, and H. Yamada, Phys. Rev. Lett. **56**, 792 (1986).
[18] R. E. Dunin-Borkowski, T. Kasama, A. Wei, S. L. Tripp, M. J. Hÿtch, E. Snoeck, R. J. Harrison, and A. Putnis, Microsc. Res. Techn. **64**, 390 (2004).
[19] F. Genz, T. Niermann, B. Buijsse, B. Freitag, and M. Lehmann, Ultramicroscopy **147**, 33 (2014).
[20] M. Paris and J. Rehacek, *Quantum State Estimation*, *Lecture Notes in Physics* (Springer, Berlin, 2004).
[21] A. I. Lvovsky and M. G. Raymer, Rev. Mod. Phys. **81**, 299 (2009).
[22] K. A. Nugent, J. Opt. Soc. Am. A **24**, 536 (2007).
[23] M. Testorf and A. W. Lohmann, Appl. Opt. **47**, A70 (2008).
[24] J. Cowley, Ultramicroscopy **41**, 335 (1992).
[25] G. Möllenstedt and H. Wahl, Naturwissenschaften **55**, 340 (1968).
[26] W. Coene, G. Janssen, M. Op de Beeck, and D. Van Dyck, Phys. Rev. Lett. **69**, 3743 (1992).
[27] E. J. Kirkland, Ultramicroscopy **15**, 151 (1984).
[28] J. Cowley, *Diffraction Physics* (Elsevier Science, Amsterdam, 1995).
[29] W. Coene, A. Thust, M. Op de Beek, and D. van Dyck, Ultramicroscopy **64**, 109 (1996).
[30] A. Thust, W. M. J. Coene, M. Op de Beeck, and D. Van Dyck, Ultramicroscopy **64**, 211 (1996).
[31] C. T. Koch, Ultramicroscopy **108**, 141 (2008).
[32] H. Rose, Optik **39**, 416 (1973).
[33] M. R. Teague, J. Opt. Soc. Am. **73**, 1434 (1983).
[34] K. Müller, F. F. Krause, A. Béché, M. Schowalter, V. Galioit, S. Löffler, J. Verbeeck, J. Zweck, P. Schattschneider, and A. Rosenauer, Nat. Commun. **5**, 5653 (2014).
[35] W. Hoppe, Acta Crystallogr. Sec. A **25**, 495 (1969).
[36] W. Hoppe and G. Strube, Acta Crystallogr. Sec. A **25**, 502 (1969).
[37] W. Hoppe, Acta Crystallogr. Sec. A **25**, 508 (1969).
[38] R. Bates and J. Rodenburg, Ultramicroscopy **31**, 303 (1989).
[39] L. Mandel and E. Wolf, *Optical Coherence and Quantum Optics* (Cambridge University Press, Cambridge, UK, 1995).
[40] A. Torre, *Linear Ray and Wave Optics in Phase Space: Bridging Ray and Wave Optics via the Wigner Phase-Space Picture* (Elsevier Science, Amsterdam, 2005).
[41] J. Park and W. Band, Found. Phys. **1**, 211 (1971).
[42] W. Band and J. Park, Found. Phys. **1**, 339 (1971).
[43] H. Kohl and H. Rose, Adv. Electron. Electron. Phys. **65**, 173 (1985).
[44] A. Lubk and J. Zweck, Phys. Rev. A **91**, 023805 (2015).
[45] P. Schattschneider and H. Lichte, Phys. Rev. B **71**, 045130 (2005).
[46] M. Vulovic, L. M. Voortman, L. J. van Vliet, and B. Rieger, Ultramicroscopy **136**, 61 (2014).
[47] E. J. Kirkland, *Advanced Computing in Electron Microscopy* (Plenum Press, New York, 1998).
[48] L. Peng, S. Dudarev, and J. Whelan, *High Energy Electron Diffraction and Microscopy*, *Monographs on the Physics and Chemistry of Materials* (Oxford University Press, New York, 2004).
[49] J. Cowley and A. Moodie, Acta Crystallogr. **10**, 609 (1957).
[50] F. Röder and A. Lubk, Ultramicroscopy **146**, 103 (2014).
[51] A. Lubk and F. Röder, Ultramicroscopy **151**, 136 (2015).
[52] H.-W. Lee, Phys. Rep. **259**, 147 (1995).
[53] F. Natterer, *The Mathematics of Computerized Tomography. Vol. 32*, *Classics in Applied Mathematics* (Society for Industrial and Applied Mathematics, Philadelphia, 2001).
[54] W. Pauli, in *Reprinted: Encyclopedia of Physics* (Springer, Berlin, 1933).
[55] F. Keinert, SIAM Rev. **31**, 273 (1989).
[56] F. Natterer and F. Wübbeling, *Mathematical Methods in Image Reconstruction* (Society for Industrial and Applied Mathematics, Philadelphia, 2001).
[57] G. Möllenstedt and H. Düker, Naturwissenschaften **42**, 41 (1955).
[58] H. Lichte and B. Freitag, Ultramicroscopy **81**, 177 (2000).
[59] J. Verbeeck, D. v. Dyck, H. Lichte, P. Potapov, and P. Schattschneider, Ultramicroscopy **102**, 239 (2005).
[60] P. Potapov, H. Lichte, J. Verbeeck, and D. van Dyck, Ultramicroscopy **106**, 1012 (2006).
[61] D. Paganin and K. A. Nugent, Phys. Rev. Lett. **80**, 2586 (1998).
[62] J. C. Petruccelli, L. Tian, and G. Barbastathis, Opt. Express **21**, 14430 (2013).
[63] C. Trahan and R. Wyatt, *Quantum Dynamics with Trajectories: Introduction to Quantum Hydrodynamics*, *Interdisciplinary Applied Mathematics* (Springer, New York, 2006).
[64] J. M. Rodenburg and R. H. T. Bates, Philos. Trans. R. Soc. London Ser. A: Phys. Eng. Sci. **339**, 521 (1992).
[65] B. McCallum and J. Rodenburg, Ultramicroscopy **45**, 371 (1992).
[66] H. N. Chapman, Ultramicroscopy **66**, 153 (1996).

[67] P. Li, T. B. Edo, and J. M. Rodenburg, Ultramicroscopy **147**, 106 (2014).
[68] Note that our purity values provided in [51] need to be multiplied with an additional factor of 2π to be consistent with the definition of the purity.
[69] J. M. Rodenburg and H. M. L. Faulkner, Appl. Phys. Lett. **85**, 4795 (2004).
[70] P. Thibault, M. Dierolf, O. Bunk, A. Menzel, and F. Pfeiffer, Ultramicroscopy **109**, 338 (2009).
[71] A. M. Maiden and J. M. Rodenburg, Ultramicroscopy **109**, 1256 (2009).
[72] P. Thibault and A. Menzel, Nature **494**, 68 (2013).
[73] K. Harada, A. Tonomura, Y. Togawa, T. Akashi, and T. Matsuda, Appl. Phys. Lett. **84**, 3229 (2004).
[74] M. Humphry, B. Kraus, A. Hurst, A. Maiden, and J. Rodenburg, Nat. Commun. **3**, 730 (2012).
[75] W. P. Schleich, *Quantum Optics in Phase Space* (Wiley VCH, Berlin, 2001).
[76] P. Jaming, Appl. Comput. Harmonic Anal. **37**, 413 (2014).
[77] R. W. Gerchberg and W. O. Saxton, Optik **35**, 237 (1972).
[78] J. R. Fienup, Appl. Opt. **21**, 2758 (1982).
[79] By this restriction we exclude techniques exploiting the characteristics of dynamic electron scattering itself from our discussion.
[80] J. Barthel and A. Thust, Phys. Rev. Lett. **101**, 200801 (2008).
[81] F. Röder and A. Lubk, Ultramicroscopy **152**, 63 (2015).
[82] P. Schattschneider, S. Rubino, C. Hebert, J. Rusz, J. Kunes, P. Novák, E. Carlino, M. Fabrizioli, G. Panaccione, and G. Rossi, Nature **441**, 486 (2006).
[83] L. J. Allen, M. P. Oxley, and D. Paganin, Phys. Rev. Lett. **87**, 123902 (2001).